



**Effect of growth dynamics on the structural, photophysical
and pseudocapacitance properties of famatinite copper
antimony sulphide colloidal nanostructures**

Journal:	<i>Dalton Transactions</i>
Manuscript ID	DT-ART-10-2024-002826.R1
Article Type:	Paper
Date Submitted by the Author:	21-Nov-2024
Complete List of Authors:	Weston, Kimberly; The University of the West Indies St Augustine Campus, Chemistry Taylor, Richard; The University of the West Indies Saint Augustine Campus, Chemistry Kisslinger, Kim; Brookhaven National Laboratory, Center for Functional Nanomaterials Mantripragada, Shobha; North Carolina Agricultural and Technical State University

SCHOLARONE™
Manuscripts

ARTICLE

Effect of growth dynamics on the structural, photophysical and pseudocapacitance properties of famatinite copper antimony sulphide colloidal nanostructuresKimberly Weston,^a Richard A. Taylor,^{*a} Kim Kisslinger,^b and Shobha Mantripragada^c

Received 00th January 20xx,
Accepted 00th January 20xx

DOI: 10.1039/x0xx00000x

Facile phase selective synthesis of copper antimony sulphide (CAS) nanostructures is important because of their tunable photoconductive and electrochemical properties. In this study, off-stoichiometric famatinite phase CAS (*f*CAS) quasi-spherical and quasi-hexagonal colloidal nanostructures (including nanosheets) of sizes, 2.4 – 18.0 nm were grown under variable conditions of temperature (60 – 200 °C), time and oleylamine capping ligand concentration using copper(II) acetylacetone and antimony(III) diethyldithiocarbamate precursors. Data from powder X-ray diffraction, Raman spectroscopy and high-resolution scanning/transmission electron microscopy confirm the tetragonal structure of the famatinite phase. X-ray photoelectron spectroscopy, transmission electron microscopy and scanning electron microscopy-energy dispersive X-ray spectroscopy data suggest a correlation of particle size, morphology and composition of the off-stoichiometric *f*CAS nanostructures with growth temperature and time, and oleylamine concentration. The off-stoichiometric $\text{Cu}_3\text{Sb}_{1+b}\text{S}_{4+c}$ (*a*, *b*, *c* – mole fractions) nanostructures are severely copper-deficient and antimony-rich in which shallow-lying acceptor copper vacancy states, deep-lying donor states of antimony interstitials, sulphur vacancies and antimony-copper antisites and shallow-lying acceptor surface trapping states are likely implicated in tunable UV-visible absorption and bandgaps between 2.3 and 2.8 eV, and broad visible-NIR photoluminescence with fast recombination of radiative lifetimes between 0.2 and 6.2 ns, confirmed from absorption, steady-state and time-resolved photoluminescence spectroscopies. Additionally, cyclic voltammetry and electrochemical impedance spectroscopy confirm that electrodes of the *f*CAS nanostructures display slightly variable pseudocapacitance of charge-storage primarily via possible sodium ion intercalation with a high specific capacitance of ~84 F g⁻¹ obtained at a scan rate of 5 mV s⁻¹. Overall, these results show the influence of composition, in particular point defects, phase quality and morphology on the optical and pseudocapacitance properties of *f*CAS nanostructures, suitable as solar absorbers or electrodes for energy storage devices.

Introduction

Transition metal chalcogenide (TMC) semiconductors are widely investigated because of their technological importance with the earth abundant copper-based ones being particularly attractive.¹ However, copper antimony sulphides (CAS) are of the least explored classes of ternary copper-based chalcogenides despite their potential.¹ The main features that make CAS interesting but challenging to investigate are their tunable electronic properties and interplay of the thermodynamic stability of the four phases: $\text{Cu}_{12}\text{Sb}_3\text{S}_{14}$ (cubic – tetrahedrite), Cu_3Sb_4 (tetragonal – famatinite), Cu_3SbS_3 (monoclinic – skinnerite), and CuSbS_2 (orthorhombic – chalcostibite).² All bulk phases distinguished by their

stoichiometry and structure^{3–6} are of p-type conductivity with tunable bandgaps between 0.5 and 2.0 eV, however, synthetic selectivity remains a challenge. Despite this, CAS phases have been investigated for a range of applications. For example, thin film solar cells of CuSbS_2 exhibit a power conversion efficiency (PCE) of 3.22 % attributed to low hole mobility ($0.1 \text{ cm}^2 \text{ Vs}^{-1}$),^{7,8,9} even though it has a bandgap of 1.38 – 1.56 eV.¹⁰ Cu_3SbS_3 , Cu_3Sb_4 and $\text{Cu}_{12}\text{Sb}_4\text{S}_{13}$ with bandgaps of 1.60 – 1.89,⁹ 0.46 – 1.85 and 1.72 eV,^{1,4,11,12} respectively, are particularly useful for photovoltaic and thermoelectric devices.⁵ Interestingly, despite its direct bandgap and high hole mobility ($0.5 – 2 \text{ cm}^2 \text{ V}^{-1} \text{ s}^{-1}$), extremely low PCEs of ~0.46 % were reported for sputtered Cu_3Sb_4 thin film solar cells.¹² Furthermore, in respect of their electron/charge transport and electrochemical properties, there is growing interest in the pseudocapacitance of CAS phases with reports of nanostructured electrodes showing surface- and diffusion-controlled, pseudocapacitive ion intercalation useful for energy storage devices.¹³ For example, electrodes of CuSbS_2 nanosheets exhibit better electrochemical performance than electrodes of two-dimensional copper molybdenum sulphide nanosheets due to their comparatively higher electronic conductivity, richer redox chemistry and high

^a Department of Chemistry, The University of the West Indies, St. Augustine, Trinidad and Tobago. *Corresponding author; richard.taylor@sta.uwi.edu

^b Center for Functional Nanomaterials, Brookhaven National Laboratory, Upton, NY, United States.

^c Department of Nanoengineering, Joint School of Nanoscience and Nanoengineering, North Carolina A&T State University, 2907 East Gate City Boulevard, Greensboro, NC 27401, USA, United States.

†Electronic supplementary Information (ESI) available: See DOI: 10.1039/x0xx00000x

ARTICLE

Journal Name

specific capacity, especially with respect to potassium ion intercalation.^{14,15} Additionally, famatinite phase CAS, i.e., Cu_3SbS_4 (*f*CAS) nanoplates prepared hydrothermally exhibit good electrode potential for supercapacitors with specific capacitance upwards of 60 F g^{-1} .¹⁶ In these cases, the surface-related pseudocapacitance of the electrodes is associated with the sheet-/plate-like morphology of the nanostructures, offering good ion intercalation kinetics.

Notwithstanding the attractive properties of CAS nanostructures, there are only few reports describing the influence of structure, composition and morphology on their optical and electrochemical properties, which therefore allows scope for further investigation. Notably, the preparation of their colloidal nanostructures often requires temperatures above $175 \text{ }^\circ\text{C}$. For example, van Embden and co-workers prepared *f*CAS nanospheres from hot-injection at $180 \text{ }^\circ\text{C}$ ¹⁷ and $\text{Cu}_{12}\text{Sb}_4\text{S}_{13}$ nanoparticles at $190 \text{ }^\circ\text{C}$.¹⁸ Ikeda and co-workers selectively prepared CuSbS_2 nanoparticles above $260 \text{ }^\circ\text{C}$, Cu_3SbS_4 nanoparticles below $200 \text{ }^\circ\text{C}$ and Cu_3SbS_3 nanoparticles via a two-step heating profile involving generation of Cu_2S and Sb_2S_3 intermediates at $150 \text{ }^\circ\text{C}$.¹⁹ Yan and co-workers prepared CuSbS_2 nanobricks at $230 \text{ }^\circ\text{C}$,²⁰ whilst Ramasamy and co-workers selectively crystallized all four phases of CAS colloidal nanostructures – CuSbS_2 nanoplates between 190 and $280 \text{ }^\circ\text{C}$, Cu_3SbS_3 platelike nanocrystals at $220 \text{ }^\circ\text{C}$, Cu_3SbS_4 oblate spheroids at $190 \text{ }^\circ\text{C}$ and $\text{Cu}_{12}\text{Sb}_4\text{S}_{13}$ hollow structures between 250 and $280 \text{ }^\circ\text{C}$.⁴ Though these high-temperature arrested precipitations are effective routes to form CAS nanoparticles,²¹ opportunities exist to explore more facile, low-temperature methods to selectively prepare colloidal nanoparticles of *f*CAS in particular,⁵ considering its kinetically-driven formation versus the thermodynamically-driven formation of its counterparts. Indeed, the selective formation of *f*CAS is challenging since its non-stoichiometric counterparts exist over a very narrow thermodynamic stability window,⁴ and in that respect its structural-, compositional-, and morphological-dependent electronic properties are generally underexplored. In this regard, the selective formation of *f*CAS nanostructures under more facile, less thermodynamically demanding and sustainable conditions would be an attractive pursuit, especially to understand their formation mechanism and importantly, the relationship of the structural, compositional, defect chemistry and morphology on the optical and electrochemical properties.

As seen from several studies,^{4,17} the growth of CAS colloidal nanoparticles typically involves the use of inorganic precursors such as chlorides and acetates as well as elemental or molecular sulphur sources which require high temperatures for decomposition and nucleation. However, metal-organic sulphur containing precursors such as metal diethyldithiocarbamates with their soft sulphur donor atoms, have proven to be very effective alternatives in phase selective growth of TMC colloidal nanoparticles, even at low temperatures. This is based on higher reactivity and low-temperature decomposition for the facile loss of the organic components enabling fast burst nucleation of binary sulphide monomer species and subsequent controlled growth of nanostructures under primarily kinetically-driven conditions.²² For example, work from this group has

involved the growth of copper indium sulphide colloidal nanoparticles using diethyldithiocarbamates over a range of temperatures, controlling their size, shape, morphology, phase transformation, composition, defect chemistry and tunable optical properties.^{23,24} This kinetically-driven colloidal mechanism using diethyldithiocarbamates provides opportunity for the phase selective growth of kinetically formed *f*CAS. Therefore, in this work, we investigate and report the phase selective growth of *f*CAS colloidal nanostructures (including nanosheets) using the versatile and robust antimony(III) diethyldithiocarbamate precursor under synergistic kinetic – thermodynamic conditions of low and high temperatures, 60 – 70 and $200 \text{ }^\circ\text{C}$, respectively, which has not been previously reported, and the effect of this on their structural, compositional, morphological and related optical and electrochemical properties. At high temperature, the effect of elemental sulphur in combination with the thiocarbamate sulphur source is investigated. Importantly, a formation mechanism based on the reactivity of the precursors is proposed considering the interplay of kinetic and thermodynamic factors influencing nanostructure growth. With this approach, the primary aim is to investigate the influence of composition and defect chemistry on the structural, optical, and electrochemical properties in reference to temperature-, time-, capping ligand- and sulphur source-dependent synthetic factors on the growth of *f*CAS nanostructures.

Results and discussion

Characterization of *f*CAS colloidal nanostructures

Fig. 1(a) shows overlaid normalized powder X-ray diffractograms of as-synthesized nanostructures grown at temperatures of 60 , 70 and $200 \text{ }^\circ\text{C}$, respectively for 30 minutes using oleylamine (OAm), sulphonated OAm (S-OAm) or a mixture of OAm and octadecene (ODE). Characteristic broad reflections (Table S1 ES[†]), typical of nanostructured particles were auto-indexed confirming the tetragonal crystal structure (ICDD reference no. 035-0581) for the famatinite phase of Cu_3SbS_4 with space group $I\bar{4}2m$ (no. 121)²⁵ and lattice constants, $a = 5.400$ – 5.985 \AA and $c = 10.820$ – 10.960 \AA .²⁶ Subtle differences in the peak positions and corresponding lattice constants suggest varying degrees of lattice distortions possibly associated with atomic ordering and intrinsic point defects, common for TMCs.²⁶ Nanostructures grown at increased temperatures of 70 and $200 \text{ }^\circ\text{C}$ (particularly) are more crystalline, evidenced from smaller full width at half maxima, slightly higher intensity, slightly higher 2θ values of the primary (112) , (004) , (204) , and (312) reflections, and presence of the (103) reflection (Table S2 ES[†]). More so, for nanostructures grown at $200 \text{ }^\circ\text{C}$, there is a slight red-shift in most reflections, a consequence of a more compact lattice, *viz.* smaller lattice constants, $a = 5.400$ – 5.410 \AA and $c = 10.800$ – 10.820 \AA . Interestingly, those grown with S-OAm at $200 \text{ }^\circ\text{C}$ are even more crystalline as evidenced from sharper, more intense reflections suggesting the influence of the additional sulphur on the growth dynamics and quality of the phase. Interestingly, the (110) reflection is now dominant, instead of the (112) , suggesting

preferred orientation effects such as more lateral domain growth relative to vertical domain growth, reflective of nanosheets.

However, for nanostructures grown at 200 °C even though highly crystalline, do not display time-dependent growth, and the ones grown at 60 °C are not crystalline enough. Therefore, since those grown at 70 °C display good crystallinity, in order to ascertain some understanding of the nanostructure growth dynamics and the effect on their structural characteristics, nanostructures were grown at 70 °C at a lower rate in reduced capping ligand concentration (2:1 mixture of OAm-ODE) over time. As shown in Fig. 1(a), Table 1 and Table S2 ESIT, a halved OAm volume fraction results in fCAS nanostructures with some structural variability. There is the expected quantum confined particle growth with time, but this occurs with reduced particle crystallinity evidenced from increasing full width at half maxima of the primary reflections, as recorded in Table S2 ESIT. Additionally, marginal shifts to lower 2θ and an increase in lattice constant, a , and unit cell volume indicates slight lattice expansion as nanostructures grown over time, possibly due to a change in the density of defects such as interstitials and antisites.²⁶ Interestingly, the ratio of the intensity of the (112) to (204) lattice reflections increases with growth time (Fig. 1 and Table S2 ESIT) suggesting preferred orientation growth effects favouring the addition of sulphur atoms along the (112) lattice plane versus addition of copper and antimony ions along the (204) lattice plane. Overall, absence of peaks associated with binary phases of copper sulphide or antimony sulphide suggests good phase purity.

Raman spectroscopy was used to further elucidate the structural characteristics of fCAS nanostructures with representative spectra shown in Fig. 1(b). However, the spectra are characterized with broad, low intensity overlapping peaks which are due in combination to the degree of crystallinity of the small nanostructures, visible photoluminescence from the oleylamine capping ligand and the related reduction of the number of active sites for Raman scattering – common for organic ligand capped nanoparticles.^{27, 28} Notwithstanding this, from group theory, five Raman-active phonon modes are expected for Cu_3SbS_4 with $I\bar{4}2m$ space group symmetry and D_{2d} point group symmetry – 4A_{1g} , 3A_{2g} , 4B_{1g} , 4B_{2g} and 6E_g .²⁹ Among these, only the A_{2g} mode is Raman inactive,³⁰ whilst the A_{1g} mode is expected to exhibit the most prominent peaks and is consistent with the behaviour observed in related stannite $\text{Cu}_2\text{FeSnS}_4$ and chalcopyrite structures.²⁹ Therefore, for nanostructures prepared using OAm at 60 °C, overlapping broad, weak peak shifts between 250 and 355 cm^{-1} correspond to the tetragonal famatinite Cu_3SbS_4 and corroborate the p-XRD data.^{5, 31} Unexpectedly, the spectrum is characterised by three dominant peaks at ~250, 302 and 350 cm^{-1} corresponding to the B_{2g} modes, which display single degeneracy and may involve asymmetric out-of-plane or in-plane bending and stretching vibrations of the Cu–S and Sb–S bonds.^{32, 33} Additionally, the symmetric stretching of the Cu–S and Sb–S bonds show Raman modes at ~271 and 312 cm^{-1} , also displaying single degeneracy attributed to the A_{1g} mode and another one at ~342 cm^{-1} corresponding to symmetric out-of-plane bending or in-plane

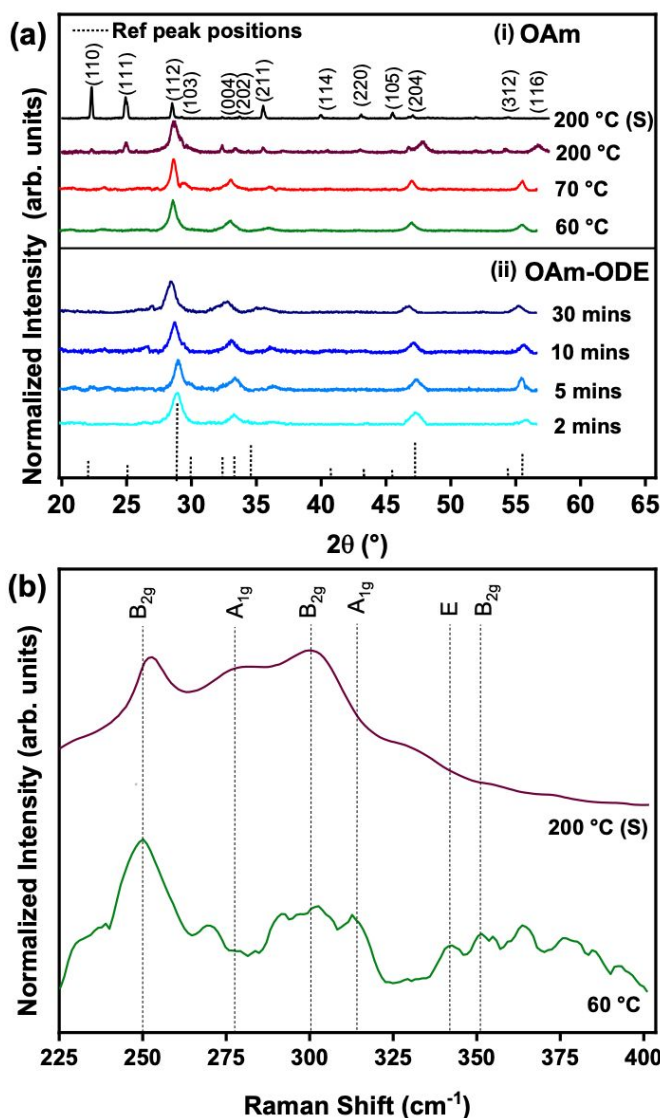


Fig. 1. (a) Overlaid powder X-ray diffractograms for fCAS nanoparticles with reference pattern showing peak positions and corresponding (hkl) values of the tetragonal crystal structure (ICDD reference no. 035-0581) for the famatinite phase of Cu_3SbS_4 ; and (b) representative Raman spectra, for fCAS nanoparticles.

bending and stretching vibrations of the Sb–S bonds of the E symmetry mode.³³ Nanostructures synthesized using S-OAm at 200 °C exhibit Raman peaks shifts at ~253, 278, 302 and 353 cm^{-1} , possibly due to shorter bond lengths. Furthermore, subtle peak shifts around 310 and 335 cm^{-1} could suggest that intrinsic defects in the crystal lattice may be causing lattice distortions by altering bond lengths.

Transmission electron microscopy (TEM) and high-resolution TEM (HR-TEM) images in Fig. 2 confirm quasi-nanospheres and quasi-hexagonal nanostructures of varying dispersity (some fairly monodispersed) of size range, $2.4 \pm 0.1 - 18.0 \pm 3.4$ nm (Table 1 and Fig. S1 ESIT), prepared using OAm at different temperatures. In particular, the TEM images of the samples grown at 200 °C show overlapping of thin sheet-like nanostructures, i.e. quasi-hexagonal nanosheets. The HR-TEM images show parallel-line like Moiré fringes suggesting some

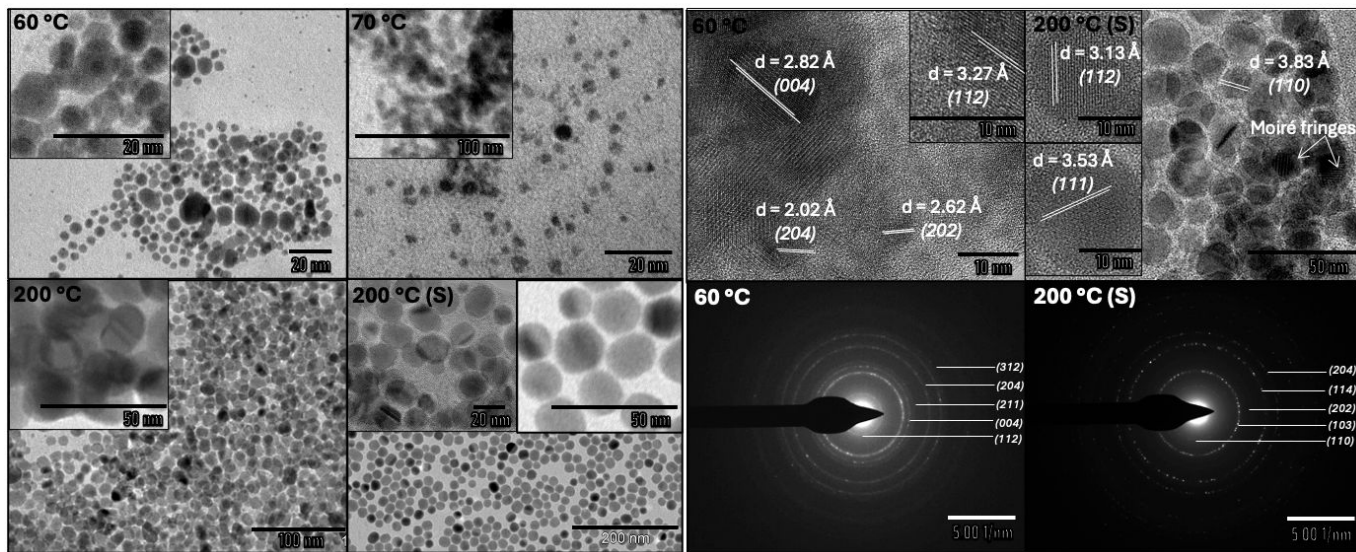


Fig. 2. Images from TEM, HR-TEM and SAED (insets) for fCAS nanostructures grown using OAm at 60, 70, 200 °C and S-OAm at 200 °C (200 °C(S)); detailed image of the Moiré fringes is Fig. S3 ESIT.

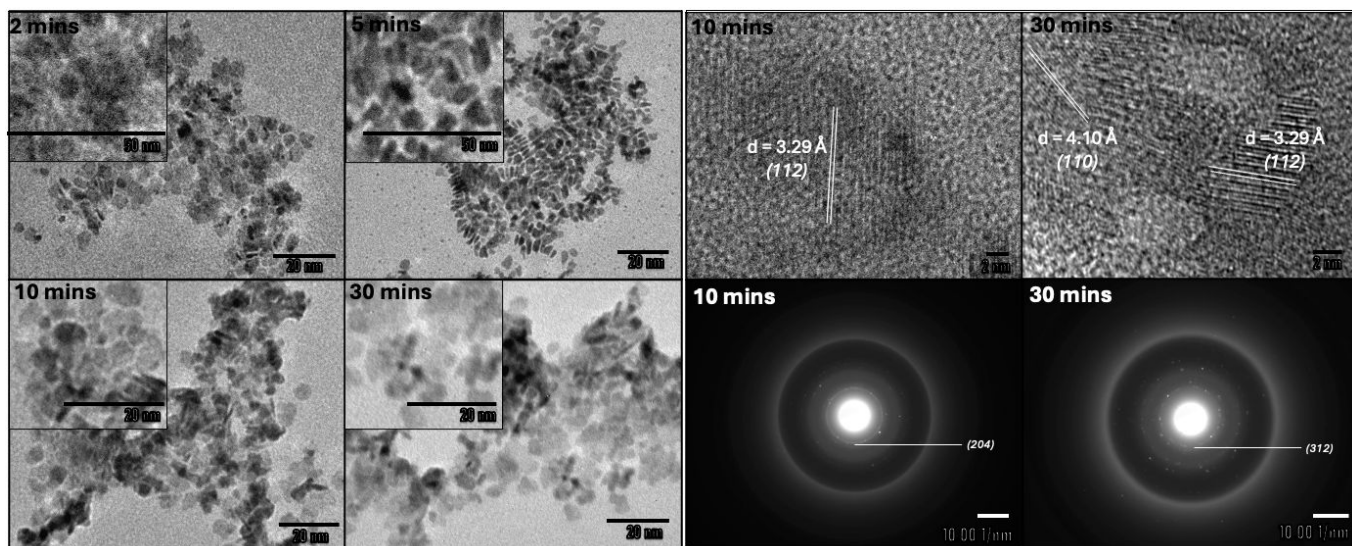


Fig. 3. Images from TEM, HR-TEM and FFT (insets) for fCAS nanostructures grown using OAm-ODE at 70 °C for 2, 5, 10 and 30 minutes.

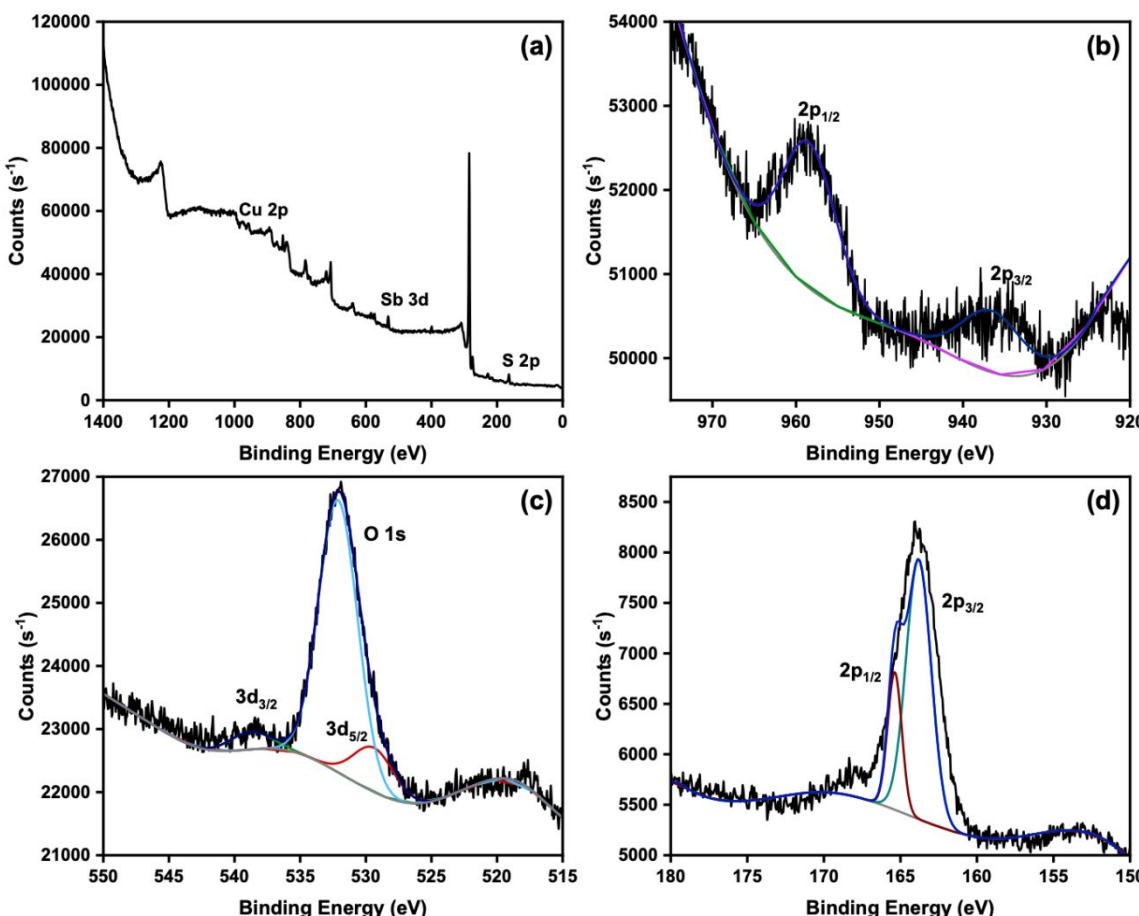
periodic stacking of the layered nanostructures (nanosheets) shown in Fig. S3 ESIT. As shown from the p-XRD data, higher growth temperatures yield larger and more crystalline nanostructures attributed to a narrower nucleation window, increased supersaturation of nuclei, and increased metal ion diffusion rates.^{1, 4, 6} As shown in Fig. 3, nanostructures grown with OAm-ODE mixture, display some time-dependent morphological change – small nanospheres (3.0 ± 1.2 nm) to slightly elongated and larger nanostructures (7.5 ± 2.5 nm) having sheet-like morphology with increased polydispersity as shown in size distribution histograms in Fig. S2 ESIT. It is likely that these time-dependent morphological changes with reduced OAm concentration are due to increased solubility of the precursors, enough to limit the nanostructure growth rate by reduced supersaturation at the nucleation and growth stages.¹⁸ This is attributed to more stable nuclei with lower

surface energy, thus suppression of the nucleation rate leading to overall larger nanostructures over time.¹⁸ Representative HR-TEM images shown in Figs. 3 and 4 for nanostructures grown for 30 minutes at 60 °C using OAm only, 200 °C using S-OAm, and 70 °C using OAm-ODE further confirm the tetragonal structure with collective lattice spacings of 4.10/3.83 (110), 3.53 (111), 3.13/3.27/3.29 (112), 2.82 (004), 2.62 (202) and 2.02 (204),^{12, 19} with representative plot profile diagram ascribed to the (112) lattice plane of fCAS nanostructures shown in Fig. S4 ESIT. Correspondingly, selected area electron diffraction (SAED) patterns in Fig. 2 show nine diffraction rings of d spacing, 3.53, 3.30, 3.10, 2.77, 2.40, 2.55, 2.20, 2.00/1.91/2.02 and 1.75/1.83 Å assigned to the (110), (112), (103), (004), (202), (211), (114), (204) and (312) lattice planes respectively, in agreement with the powder X-ray diffractograms, and further confirm the tetragonal crystal structure. Fast Fourier transform (FFT) images

Table 1. Structural information for fCAS nanostructures derived from p-XRD, TEM, HR-TEM and EDS, in reference to their colloidal growth conditions.

Nanoparticle stoichiometry	Growth temperature/°C	Growth time/minute	OAm Volume Fraction, V_f	Lattice parameters		Lattice spacing, d Å	Particle size/nm (RSD/%)
				a Å	c Å		
$\text{Cu}_{1.6}\text{Sb}_{2.0}\text{S}_{4.4}$	60	30	1.0	5.850	10.960	3.30	3.28
$\text{Cu}_{1.8}\text{Sb}_{2.1}\text{S}_{4.0}$	70	30	1.0	5.855	10.930	3.30	-
$\text{Cu}_{2.5}\text{Sb}_{1.4}\text{S}_{4.1}$	200	30	1.0	5.410	10.820	3.12	-
$\text{Cu}_{1.5}\text{Sb}_{2.7}\text{S}_{3.8}$	200 (S)	30	1.0	5.400	10.800	3.13	3.16
$\text{Cu}_{2.4}\text{Sb}_{1.8}\text{S}_{3.7}$	70	2	0.5	5.800	10.880	3.27	-
$\text{Cu}_{2.5}\text{Sb}_{1.9}\text{S}_{3.6}$	70	5	0.5	5.795	10.880	3.26	-
$\text{Cu}_{2.2}\text{Sb}_{2.2}\text{S}_{3.6}$	70	10	0.5	5.815	10.960	3.29	3.29
$\text{Cu}_{2.8}\text{Sb}_{2.2}\text{S}_{3.0}$	70	30	0.5	5.985	10.865	3.34	-

-Corresponds to not measured or calculated; V_f = volume of OAm / (volume of OAm + volume of ODE)

**Fig. 4.** Representative XPS spectra showing Gaussian peak deconvolutions for fCAS nanostructures synthesized at 70 °C for 30 minutes using OAm only: (a) survey; (b) Cu 2p; (c) Sb 5d; and (d) S 2p.

in Fig. 3 also correlate with the tetragonal structure. Additionally, energy dispersive X-ray spectroscopic (EDS) data confirm off-stoichiometric copper-poor and antimony-rich nanostructures of the general formula, $\text{Cu}_{3-a}\text{Sb}_{1+b}\text{S}_{4\pm c}$ (a, b, c – mole fractions) (Table 1 and S3 ESIT). Representative elemental mapping and high-angle annular dark field (HAADF) imaging of nanostructures synthesized with OAm at 60 °C and S-OAm at

200 °C (200 °C (S)) are shown in Figs. S5 and S6 ESIT and confirm uniform element distribution within the nanostructures. Overall, since the off-stoichiometric phases exist over a very narrow thermodynamic stability window,⁴ the particle quality is largely dependent on kinetic factors influencing growth mechanisms at notably low growth temperatures of 60 and 70 °C, with those grown at 200 °C exhibiting the best phase purity,

ARTICLE

Journal Name

demonstrating the effectiveness of higher temperatures in achieving phase selectivity.

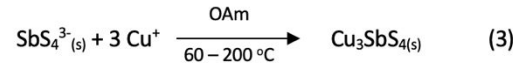
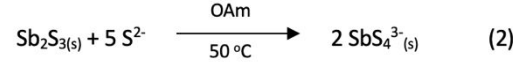
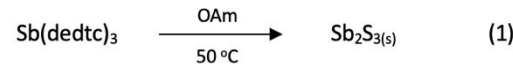
Furthermore, X-ray photoelectron spectroscopic (XPS) data confirm the presence of the Cu^+ , Sb^{5+} , and S^{2-} species in the fCAS nanostructures. Representative spectra in Fig. 4 with binding energies shown in Table S4 ESIT indicate $\text{Cu} 2\text{p}_{3/2}$ and $\text{Cu} 2\text{p}_{1/2}$ states with binding energies at ~ 939 , and ~ 959 eV, respectively and peak splitting energy of ~ 20 eV expected for Cu^+ ions^{23, 34, 35} with no satellite peaks.^{35, 36} Additionally, deconvoluted $\text{Sb} 3\text{d}_{5/2}$ and $3\text{d}_{3/2}$ peaks with binding energies of ~ 531 and ~ 539 eV of peak splitting energy of ~ 9.0 eV, confirm Sb^{5+} . Typically, $\text{Sb} 3\text{d}_{3/2}$ spectral line is around 540 eV, which is consistent with this data and confirms Sb^{5+} .¹⁷ Additionally, there are binding energies for $\text{S} 2\text{p}_{3/2}$ at ~ 164 eV and $2\text{p}_{1/2}$ at ~ 165 eV with peak splitting at ~ 1.0 eV³⁷. Additionally, the $\text{O} 1\text{s}$ peak with binding energy of ~ 532 eV confirms the presence of oxygen from surface oxidation which isn't uncommon for chalcogenides due to handling in air.³⁸

Nanostructure formation and growth mechanism

Optimization of the synthetic approach through an understanding of the formation and growth mechanism for TMC colloidal nanostructures is instrumental in tailoring their properties. In this respect, it has been reported that the formation of Cu-III-VI chalcogenide colloidal nanoparticles can occur via cation exchange of M^{3+} (M = metal) of *in situ* metal sulphide (M_2S_3) nanoparticles with Cu^+ or thermolysis of an *in situ* Cu-M thiolate precursor.^{23, 39, 40} In this work, a feature of the former mechanism is more likely for fCAS nanostructures considering their kinetically-driven formation due to the low-temperature (50 °C) decomposition of the antimony(III) diethyldithiocarbamate precursor, forming antimony sulphide (Sb_2S_3) nanoparticles in oleylamine (OAm) rendering high availability of Sb^{3+} .⁵ Here, formation of Sb_2S_3 is confirmed from p-XRD analysis, where auto-indexing confirms the orthorhombic crystal system (ICDD reference no. 00-006-0474) typical for Sb_2S_3 (Table S1, S3 and Fig. S7 ESIT), and EDS analysis which confirms the stoichiometry of nanoparticle samples isolated from suspended reactions without injection of the copper precursor. Subsequent hot-injection of the copper precursor results in reduction of Cu^{2+} to Cu^+ by the OAm reducing agent. Notably, Baum, Pretto and co-workers,^{40, 41} based on a design of experiments approach reported that selective formation of fCAS colloidal nanoparticles results from a reaction medium consisting of OAm, excess sulphur and impurities of oxygen as antimony oxide (Sb_2O_3) formed in an initial step by hydrolysis with OAm. This leads to the formation of an intermediate phase, SbS_4^{3-} , involving oxidation of Sb^{3+} to Sb^{5+} – the valency of antimony in the famatinite phase. In this work, similar conditions exist with excess sulphur (S^{2-}) available from the diethyldithiocarbamate precursor (and added elemental S at 200 °C), acting as an oxidizing agent. As such, the early stage formation of Sb_2S_3 in the presence of sulphur oxidizing agent and OAm (weak reducing agent) results in the formation of SbS_4^{3-} nanostructures, with subsequent incorporation of Cu^+ into their primordial lattice at a rate

comparable to their formation, leading to growth of the ternary lattice.¹⁸ Accordingly, we propose in Scheme 1, a step-wise formation mechanism for the fCAS colloidal nanostructures.

Additionally, FTIR spectra (Fig. S8 ESIT) confirm OAm capping ligands on the fCAS colloidal nanostructures with characteristic modes of $\nu_s(\text{C}-\text{H}_2) - 2851$, $\nu_{as}(\text{C}-\text{H}_2) - 2925$, $\nu(\text{C}-\text{H})$ of the C-H bond adjacent to the C=C bond – 3005, $\nu_s(\text{C}=\text{C}) - 1653$, $\nu_{sc}(\text{N}-\text{H}_2) - 1573$, and $\nu_s(\text{N}-\text{H}) - 3300$ cm^{-1} . Notably, the presence of the amine modes confirm that OAm bonds with cations of certain facets of the fCAS nanostructures through electron donation from the nitrogen atom of the NH_2 group.⁴² In this formation mechanism, OAm acts as a (i) coordinating ligand and interacts with the metal precursors to induce nanoparticle nucleation, (ii) reducing agent for Cu^{2+} , and (iii) surfactant, controlling nanoparticle growth, and preventing their aggregation through reduced surface tension and increased repulsive forces due to steric exclusion.^{39, 40} Indeed, the off-stoichiometric phase of the fCAS nanostructures is attributed to conditions involving the tendency of their growth over time towards thermodynamic stability. However, with the XPS data confirming no Sb^{3+} ions, it appears that the conditions such as the inability for the weak OAm reducing agent to reconvert Sb^{5+} to Sb^{3+} limit transformation of the fCAS phase to the more thermodynamically stable CuSbS_2 phase, and therefore the off-stoichiometry is attributed to some degree of lattice disorder associated with a range of point defects. Notwithstanding, low-temperature precursor decomposition enables growth at variable temperatures with excess sulphonating agent providing optimum conditions for precipitation of fCAS colloidal nanostructures including



Scheme 1. Formation of Cu_3SbS_4 nanostructures including off-stoichiometric fCAS nanostructures.

nanospheres and nanosheets – the latter resulting at 200 °C from excess sulphur promoting more lateral domain (110) growth over vertical domain growth, evidenced from the p-XRD.

Absorption and photoluminescence properties

Particle size-, composition- and phase-dependent tunable optical properties of fCAS colloidal nanostructures are attractive for electronic applications. Accordingly, the as-synthesized nanostructures exhibit strong visible absorption⁴ as shown from UV-vis spectra in Fig. 5(a) and (b). Interestingly, the spectra and corresponding Tauc plots (Ahv^2 versus hv) display Urbach tails typically associated with intra bandgap states, characteristic of defected, doped, and bulk or surface modified semiconductors.⁸⁰ Therefore, a method⁴³ involving the intersection of linear fits above and below the fundamental

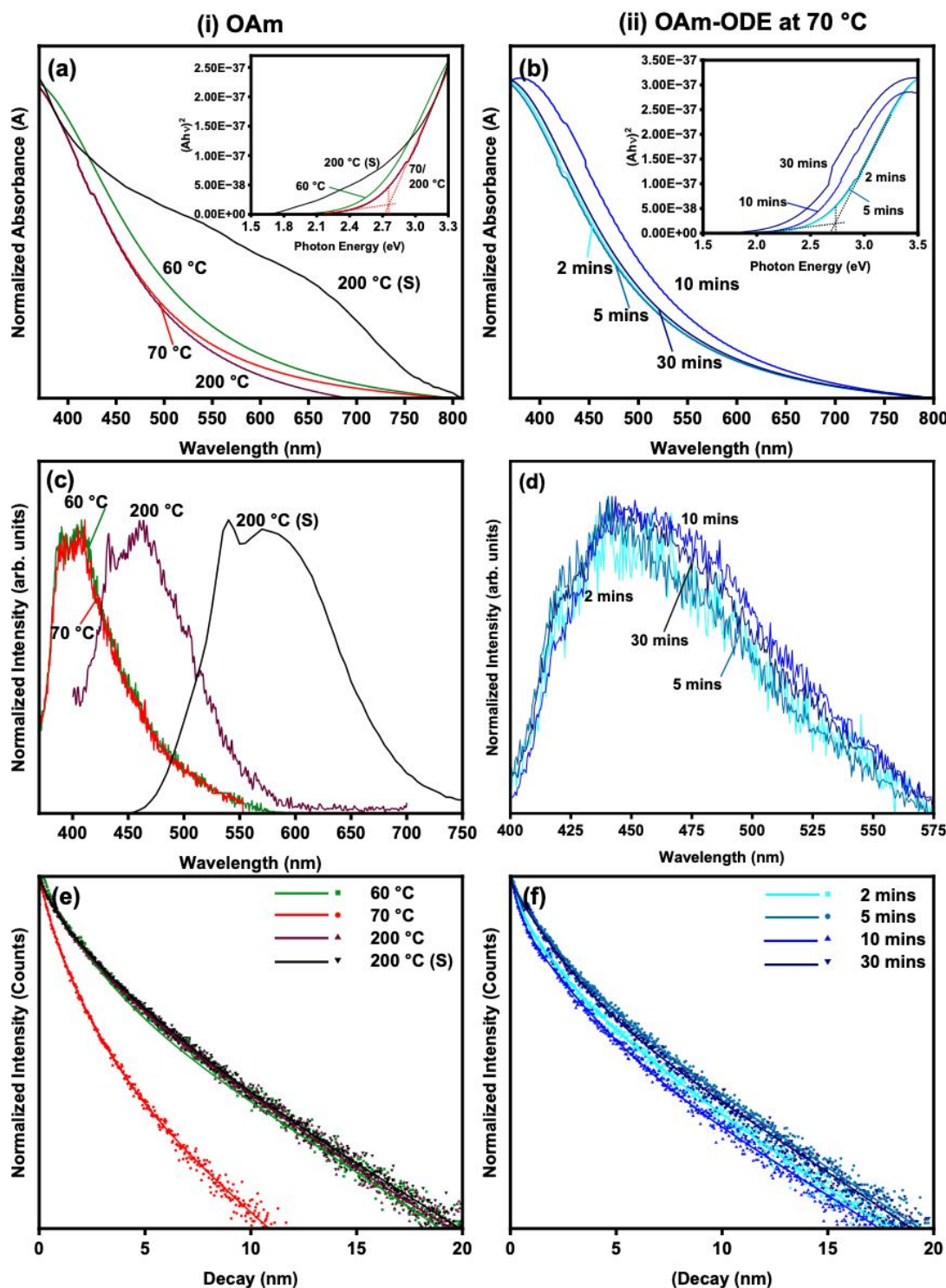


Fig. 5. For fCAS nanostructures synthesized respectively using (i) OAm at 60, 70, 200 °C and S-OAm at 200 °C (S) and (ii) OAm-ODE mixture for 2, 5, 10, and 30 minutes: (a) and (b) overlaid UV-Vis absorption spectra (inset – corresponding Tauc plots); (c) and (d) corresponding overlaid photoluminescence (PL) spectra – excitation wavelength, λ_{ex} of 350 nm – OAm at 60 and 70 °C, and OAm-ODE mixture for 2, 5, 10, and 30 minutes, λ_{ex} of 370 nm – OAm at 200 °C, and λ_{ex} of 425 nm – S-OAm at 200 °C (S); (e) and (f) corresponding overlaid time-resolved PL decay curves.

absorption is employed to more accurately estimate the bandgap. As expected, due to particle size quantum confinement, nanostructures synthesized at 60 and 70 °C with OAm only, display fairly wide direct bandgaps of 2.67 and 2.75 eV, respectively. Interestingly, the much larger nanosheets

grown at 200 °C using OAm have a wider than expected direct bandgap of 2.76 eV, and a narrower one of 2.58 eV for those grown using S-OAm. This suggests stoichiometric differences (Table 2) associated with native defects influencing the valence and conduction band density of states.^{11, 44} Additionally, fCAS

Table 2. Summary of absorption, steady-state and time-resolved photoluminescence spectroscopic data of fCAS nanoparticles.

Nanoparticle Stoichiometry	Absorption/eV	Emission/nm	Emission peak deconvolution						Radiative decay					
			^a P ₁ /nm	^b F ₁ /%	^a P ₂ /nm	^b F ₂ /%	^a P ₃ /nm	^b F ₃ /%	τ ₁ /ns	A ₁ /%	τ ₂ /ns	A ₂ /%	τ ₃ /ns	A ₃ /%
Cu _{1.6} Sb _{2.0} S _{4.4}	2.67	385, 402, 425	385	03.7	402	29.6	425	66.7	2.68 ± 0.7	45.2	0.74 ± 0.3	27.0	6.16 ± 0.5	27.8
Cu _{1.8} Sb _{2.1} S _{4.0}	2.75	385, 402, 427	385	03.9	402	31.3	427	64.8	1.67 ± 0.0	39.9	0.60 ± 0.0	51.7	4.55 ± 0.2	08.5
Cu _{2.5} Sb _{1.4} S _{4.1}	2.76	439, 472, 496	439	48.6	472	08.8	496	42.6	2.43 ± 1.7	41.4	0.63 ± 0.7	32.5	5.94 ± 2.7	26.1
Cu _{1.5} Sb _{2.7} S _{3.8}	2.58	537, 594, 610	537	27.8	594	24.1	610	48.1	1.78 ± 0.4	31.5	0.24 ± 0.4	30.1	5.32 ± 0.2	38.4
Cu _{2.4} Sb _{1.8} S _{3.7}	2.69	396, 428, 476	396	19.0	428	39.9	476	41.1	1.69 ± 1.7	47.6	0.35 ± 0.7	19.6	5.29 ± 2.5	32.8
Cu _{2.5} Sb _{1.9} S _{3.6}	2.71	397, 430, 476	397	20.7	430	37.0	476	42.3	1.88 ± 1.5	49.1	0.48 ± 1.7	15.2	5.43 ± 2.8	35.7
Cu _{2.2} Sb _{2.2} S _{3.6}	2.55	400, 433, 474	400	20.0	433	33.8	474	46.2	1.52 ± 1.4	48.7	0.25 ± 0.6	24.9	5.21 ± 2.0	26.3
Cu _{2.8} Sb _{2.2} S _{3.0}	2.39	396, 432, 476	396	27.1	432	36.8	476	36.1	1.80 ± 1.6	41.4	0.55 ± 0.8	34.1	5.61 ± 3.1	24.6

^aP₁ (peak 1), P₂ (peak 2) and P₃ (peak 3) are related to τ₁, τ₂ and τ₃, and A₁, A₂ and A₃, though not necessarily directly; ^bF corresponds to peak fraction; - corresponds to not measured/calculated; * corresponds to peak shoulders.

nanostructures prepared using the OAm-ODE mixture exhibit quantum confined red-shifted visible absorption from 2.71 to 2.39 eV, as recorded in Table 2. Overall, these bandgaps are significantly wider than the bulk bandgap of 0.47 eV¹⁷ for Cu₃SbS₄ and previously reported nanocrystals of size 10.2 ± 1.1 nm (0.9 – 1.2 eV).^{4, 17} However, they correlate well with a fundamental bandgap of ~2.5 eV for oblate spheroids of Cu₃SbS₄ nanoparticles calculated from density-functional theory (DFT) performed within the generalized gradient approximation of Perdew, Burke, and Ernzerhof and the screened hybrid-functional method of Heyd, Scuseria, and Ernzerhof.⁴

Correspondingly, steady-state and time-resolved photoluminescence (PL) spectroscopies provide additional insights regarding the electronic transitions responsible for the optical properties. It is important to note that three excitation wavelengths, 350, 370 and 425 nm were used to collect emission spectra for fCAS nanoparticles grown using OAm at 60 and 70 °C, and S-OAm at 200 °C(S), respectively. As shown in Fig. 5(c) and (d), both sets (OAm and OAm-ODE) of nanostructures exhibit broad PL emission within the range, 370 – 750 nm. Gaussian deconvolution of the peaks indicates three components, P₁, P₂, and P₃, as shown in Table 2 which may suggest that there are three routes associated with exciton recombination. However, the emission bands for both sets of samples display distinct features. For nanostructures grown from OAm only at 60 and 70 °C, there is a doublet at ca. 385 and 400 nm and a slight shoulder at ca. 425 nm. However, for nanosheets grown at 200 °C, the emission is red-shifted with a doublet and a distinct shoulder at 439, 472 and 496 eV, respectively, reflecting the influence of density of states associated with the copper-poor and antimony-rich composition on the electronic band structure. A notable red-shift is observed for nanosheets grown at 200 °C using S-OAm with two distinct emission peaks at ca. 540 and 590 nm and a less obvious shoulder at ca. 620 nm, attributed to increased particle sizes. Additionally, in comparison to nanostructures grown from OAm only at 70 °C, those prepared with OAm-ODE display slightly red-shifted emission with maximum ca. 398 nm

and shoulders ca. 430 and 475 nm. Though particle size effects may be a factor, it is more likely that these emission characteristics are related to composition dependent electronic states of point defects. Considering the generally copper- and sulphur-deficient, and antimony-rich compositions, the likely defects are shallow-lying acceptor states of copper vacancies, V_{Cu}, deep-lying donor states of sulphur vacancies, V_S, antimony interstitials, Sb_i and antimony-copper antisites, Sb_{Cu}.⁴⁵ The interesting, uncharacteristic doublet or shoulder features suggest competing mechanisms of electron–hole recombination. The broad emissions could be associated with the size distribution (RSD = 11 – 42 %),⁵² but the doublet/shoulder feature in particular may suggest emission more likely associated with a combination of intra-bandgap surface states and intrinsic defect states involving donor–acceptor pairs (DAPs) rather than band to band transitions.^{23, 24, 46–49} Generally, the full width at half maximum (FWHM) values for deconvoluted PL peak 1 is narrowest (~11 – 67 nm) and broadens for peaks 2 (~41 – 73 nm) and 3 (~84 – 137 nm,) respectively. Importantly, particles grown at lower

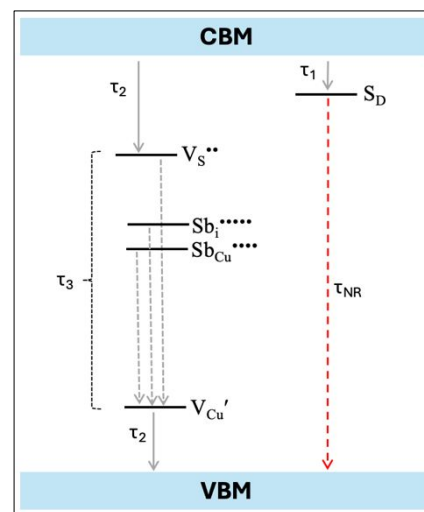


Fig. 6. Proposed electronic band diagram showing possible recombination pathways for fCAS nanostructures. Radiative lifetimes, τ₁, τ₂ and τ₃ are associated with recombinations.

temperatures exhibit narrower FWHM, whilst those grown at higher temperatures show broader and more uniform FWHM values.^{50, 51} These may likely be attributed to differences in particle sizes and the presence of intrinsic defects.⁵²

Additionally, photoluminescence decay curves shown in Fig. 5(e) and (f) fit well to a tri-exponential function of the form, $I_{PL}(t) = I_0 + A_1 e^{-t/\tau_1} + A_2 e^{-t/\tau_2} + A_3 e^{-t/\tau_3}$, with τ_1 , τ_2 and τ_3 representing radiative lifetimes, and A_1 , A_2 and A_3 , their respective components. The I_0 term is likely associated with non-radiative decay with a lifetime constant of τ_{NR} as illustrated in Fig. 6. The radiative lifetimes, τ_1 , τ_2 and τ_3 are 0.2 – 0.7, 1.5 – 2.7 and 4.6 – 6.2 ns, respectively (Table 2). As illustrated in Fig. 6, the 0.2 – 0.7 ns decay is assigned to transition between band edges and shallow surface trapping states, S_D , of faster decay lifetimes compared to intrinsic recombination of populated core states, which are assigned to 1.5 – 2.7 ns.⁸ The longest lifetime, τ_3 of 4.6 – 6.2 ns is likely related to transitions between internal defect states such as DAPs (V_{Sb} , Sb_i and Sb_{Cu} to V'_{Cu}). Corresponding amplitude constants A_1 , A_2 and A_3 which range from 31.5 – 49.1, 15.2 – 51.7 and 8.5 – 38.4 %, respectively, indicate that the most dominant radiative recombination channels involve the decays between band edges and intrinsic defects with transition between DAPs contributing significantly less to the luminescence.

Pseudocapacitance properties

The behaviour of solid-state electrodes of *f*CAS colloidal nanostructures for electrochemical energy storage applications was studied using cyclic voltammetry (CV) and electrochemical impedance spectroscopy (EIS) using a three-electrode configuration in an aqueous solution of 1 M Na₂SO₄ as the electrolyte. There appears to be some relationship of the nanostructures and electrochemical behaviour of the as-prepared electrodes. For example, as shown in Fig. 7(a), the shape of representative cyclic voltammograms for an electrode prepared from nanospheres grown using OAm at 60 °C (electrode-OAm-60) obtained from increasing scan rates between 0.005 and 0.500 V s⁻¹ in the potential range of -1.1 to 0.5 V depict a quasi-rectangular behaviour with indistinct cathodic shoulders observed at ca. -0.6 V, and anodic peaks at ca. -0.3, -1.0, and +0.1 V. This suggests irreversible Faradaic redox reactions involving partial/minimal reduction of Cu⁺ to Cu_(S) and partial/minimal oxidation of Cu_(S) to Cu²⁺, SO_{4(aq)}²⁻ + H₂O_(l) to SO_{3(aq)}²⁻ + OH_(aq)⁻, and Cu⁺ to Cu²⁺, respectively, at the electrode surface during the scan cycle.¹⁶ Additionally, as scan rate increases, there are two observations in the anodic and cathodic traces, both indicative of pseudocapacitance behaviour: (i) shifts to higher and lower potentials, respectively, indicating better polarization and faster electron transfer processes on the electrode's surface, and (ii) the current range increases linearly with the square root of scan rate, due to reduced surface reactions and diffusion-limited intercalation, possibly of the Na⁺ ions.⁵³ Importantly, the R² values for the correlations are 0.9797 and 0.9994, respectively for electrode-OAm-60 and S-OAm-200. These correlations are similar to previous reports involving intercalation of Na⁺ ions.^{14, 54}

Therefore, pseudocapacitance involves a combination of partial/minimal surface redox Cu⁺/Cu_(S), Cu_(S)/Cu²⁺ and SO_{4(aq)}²⁻ + H₂O_(l) / SO_{3(aq)}²⁻ + OH_(aq)⁻, and possibly surface related reversible diffusion-assisted intercalation of Na⁺ ions between the electrolyte and the electrode.¹⁴ Here, during the charging process, the Na⁺ ions from the electrolyte intercalate the electrode and liberate an electron, whereas during discharging, Na⁺ ions de-insert from the *f*CAS electrode. On the contrary, voltammograms shown in Fig. 7(b) for the electrode made from nanosheets grown using S-OAm at 200 °C (electrode-S-OAm-200) at increasing scan rates between 0.005 and 0.1 V s⁻¹, depict a distinct rectangular behaviour with no redox peaks, suggesting better pseudocapacitance involving morphologically-dependent reversible diffusion-assisted intercalation of possible Na⁺ ions between the electrolyte and electrode, which improves with increasing scan rate, evidenced from the shifts to higher and lower oxidation and reduction scan potentials and an increase in the current range. Additionally, for both *f*CAS electrodes, an increase in the peak separation potential (ΔE), determined using the maximum and minimum peaks at ca. -0.3 and -1.0 V, respectively, with an increase in scan rates suggests electrochemical irreversibility. Furthermore, the specific capacitance, C_{sp} of the *f*CAS electrodes was calculated using the cyclic voltammetry data.^{14, 16} At a scan rate of 5 mV s⁻¹, maximum C_{sp} is 80.9 and 83.6 F g⁻¹ for electrode-OAm-60 and electrode-S-OAm-200, respectively. Fig. 7(e) and (f) shows a decrease in C_{sp} with increasing scan rate for the respective *f*CAS electrodes – retaining ca. 50 % (40.3 F g⁻¹) and 28 % (23.5 F g⁻¹), respectively, of initial value with a twenty-fold increase in scan rate, and suggests limited mass transport of Na⁺ ions at the higher scan rates.¹⁶ Interestingly, these *f*CAS electrodes offer improved pseudocapacitance over electrodes made from layered *f*CAS nanoplates of 50 – 100 nm (prepared hydrothermally), as reported by Mariappan and co-workers with C_{sp} between 20 and 60 F g⁻¹ involving Li⁺ ion diffusion.^{4, 16} but much lower than solvothermally prepared microflowers composed of nanosheets which exhibit extremely high C_{sp} of 1423 F g⁻¹.⁵⁵ Relatively, layered CuSbS₂ nanoplates possess C_{sp} of 120 F g⁻¹ using LiOH electrolyte.⁵⁶ Generally, the other phases of Cu-Sb-S crystallize in non-layered structures, not suitable for charge storage applications, resulting in much lower specific capacitance in KOH and LiOH.⁵⁵ Certainly, as with our *f*CAS nanostructures, the surface-related pseudocapacitance of the electrodes is associated with the sheet-/plate-like morphology of the nanostructures, offering good ion intercalation kinetics.

Furthermore, to investigate the charge transfer kinetics and evaluate the capacitive dynamics of the *f*CAS electrodes, electrochemical impedance spectroscopic (EIS) analysis was performed at a frequency range of 0.1 – 100 kHz with amplitudes of 0.005 V, at fixed electrode potentials of 0.0 and 0.5 V. The Nyquist plots in Fig. 7(g) and (h) for the *f*CAS electrodes signify the frequency response of the electrode/electrolyte interface. For the electrode-OAm-60, the plots show that with an increase in applied potential, the straight Warburg line deviates from the imaginary (-Z') which is

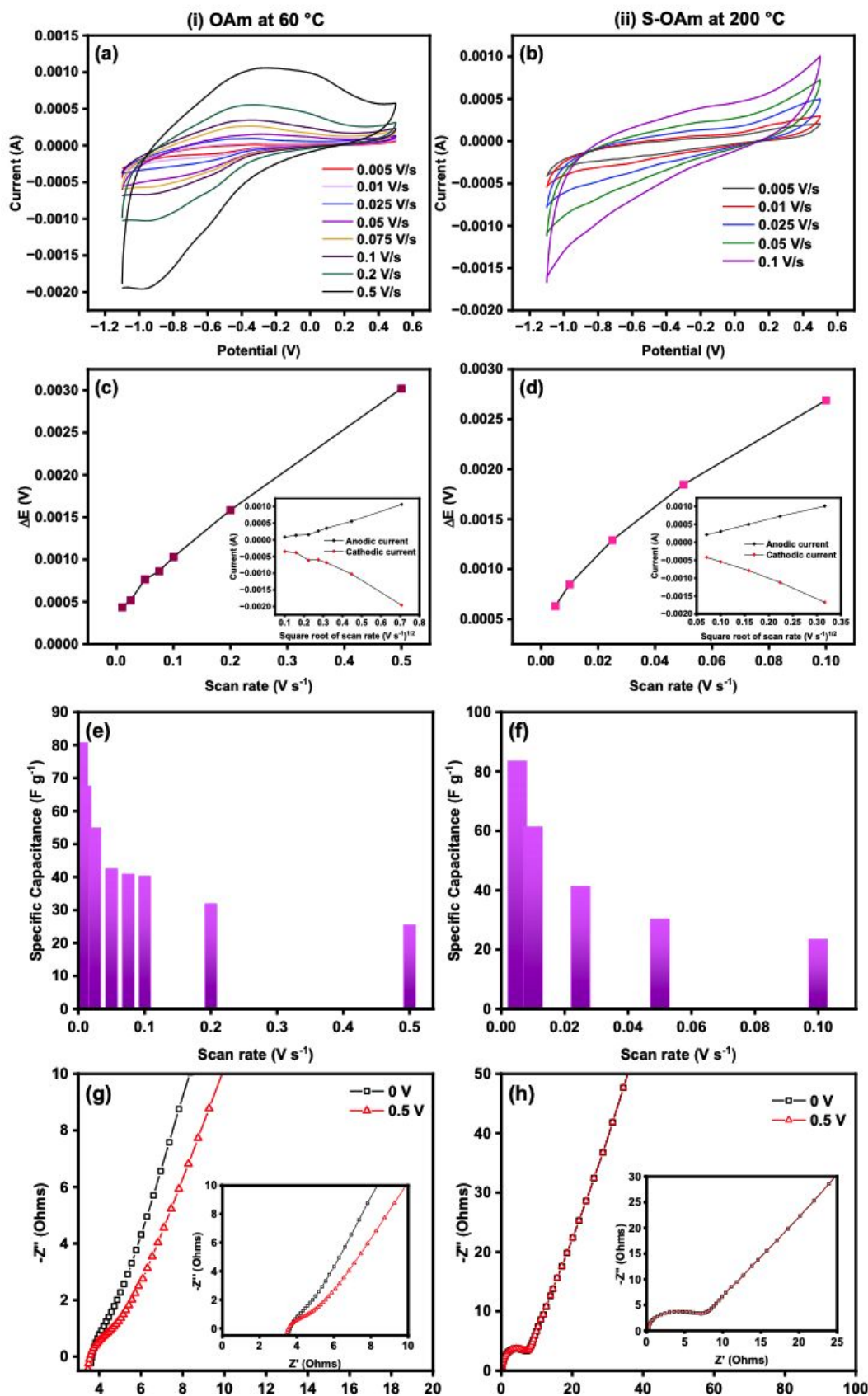


Fig. 7. Electrochemical performance of representative (i) electrode-OAm-60 and (ii) electrode-S-OAm-200, prepared from respective fCAS nanostructures, showing: (a) and (b) cyclic voltammograms; (c) and (d) plots of peak separation potential (ΔE) versus scan rates (inset – plots of anodic and cathodic current versus scan rate); (e) and (f) specific capacitance versus scan rate; (g) and (h) Nyquist plots.

attributed to faster Na^+ diffusion in the electrode material

attributed to faster Na^+ diffusion in the electrode material representing a higher contribution to the pseudocapacitance.⁵⁷ On the contrary, the Nyquist plots for the electrode-S-OAm-200 are characterized with a semicircle in the low-frequency region, typical for an ideal conductor of minimal charge transfer resistance, followed by the almost vertical Warburg line which suggests frequency dependent diffusion kinetics of the Na^+ ion intercalation and almost an ideal capacitive nature of the fCAS electrode-S-OAm-200. Additionally, unlike the electrode-OAm-60, the Nyquist plots for electrode-S-OAm-200 show no applied voltage dependence suggesting no change in Na^+ diffusion kinetics and overall good pseudocapacitance. However, the wider range of frequency for the fCAS electrode-S-OAm-200 suggests a wider range and higher rate of Na^+ ion diffusion contributing to the pseudocapacitance. The insets in Fig. 7(g) and (h) show a magnified region of the Nyquist plots, from which solution resistance, R_s of the fCAS electrodes is ~ 3.5 and $0\ \Omega$, respectively, signifying good ionic conductivity evaluated on the basis of the Randles equivalent circuit model. Additionally, the charge transfer resistances, R_{ct} are ~ 22 and $\sim 234\ \Omega$, respectively, and the bulk conductivity, R_b values of the electrodes are ~ 26 and $\sim 234\ \Omega$, respectively, attributed to lower energy losses.

Overall, the pseudocapacitance behaviour which is similar in both cases can be attributed to the sheet-like morphology of the nanostructures, wherein their layered topology facilitates ion intercalation. It can be suggested that the difference in the rate of pseudocapacitance mechanism between both electrodes, relates to the difference in nanoparticle size, morphology and crystallinity, with the larger, more crystalline quasi-hexagonal nanosheets of the electrode-S-OAm-200 providing larger surface area for enhanced rate of Na^+ diffusion compared to the smaller quasi-nanospheres of the electrode-OAm-60. The partial/minimal redox processes for the electrode-OAm-60 could be related to less effective capping ligand passivation which exposes copper ion facets more readily to the electrolyte environment. Overall, the good electrochemical performance suggests that the pseudocapacitive electrodes of fCAS colloidal nanomaterials are promising candidates for solid-state energy storage applications.

Experimental

Materials

Antimony(III) diethyldithiocarbamate, $\text{Sb}(\text{dedtc})_3$ was prepared according to a literature method.⁵⁸ Copper(II) acetylacetone ($\text{Cu}(\text{acac})_2$, Aldrich, $\geq 99.90\%$), antimony(III) iodide (SbI_3 , Aldrich, $\geq 98.00\%$), sodium diethyldithiocarbamate trihydrate (Nadedtc.3 H_2O , Aldrich, $\geq 99.99\%$), sulphur (S, Aldrich, 99.99%), oleylamine (OAm, Aldrich, $> 70.00\%$), 1-octadecene (ODE, Aldrich, 90.00%), N-methyl pyrrolidone (NMP, Aldrich, 99.50%), carbon black (CB, Aldrich, $\geq 95.00\%$), polyvinylidene fluoride (PVDF, Aldrich, average molecular weight $\sim 534,000$ by gel permeation chromatography), and sodium sulphate (Na_2SO_4 , Aldrich, 99.00%) were used without further purification, while acetone and toluene were distilled and dried using standard methods.

Synthesis of antimony(III) diethyldithiocarbamate precursor

SbI_3 (13.2 mmol, 6.6300 g) was dissolved in reagent alcohol and added dropwise to a stoichiometric amount of Nadedtc.3 H_2O dissolved in 200 mL of distilled water with constant stirring. $\text{Sb}(\text{dedtc})_3$ crystals were obtained by filtration, washed repeatedly with cold water and reagent alcohol, and recrystallized from toluene with cold hexane. The filtrate was collected, then concentrated, and small volumes of cold hexane added to precipitate crystals. $\text{Sb}(\text{dedtc})_3$: Infrared (IR) (ν_{max} , cm^{-1}): 2970–2871 ($\nu_{\text{as}}\text{C–H}$), 1487 ($\nu_{\text{as}}\text{C–N}$), 1354 ($\nu_{\text{as}}\text{C–S}$), 982 ($\nu_{\text{s}}\text{C–S}$) shown in Fig. S9 ESIT.⁵⁹ Proton nuclear magnetic resonance, ^1H -NMR (600 MHz, CDCl_3 , δ /ppm): 3.85 (q, 2H, 2 \times NCH_2 , 8.01 Hz), 1.29 (t, 3H, 2 \times CH_3 , 13.20 Hz). Carbon nuclear magnetic resonance, ^{13}C -NMR (600 MHz, CDCl_3 , δ /ppm): 199.09 (S_2C), 48.33 (NCH_2), 12.30 (CH_2) shown in Fig. S10(a) and (b) ESIT.⁶⁰

Preparation of fCAS nanostructures

In a routine synthesis, the first step involves vacuum then heating a mixture of $\text{Sb}(\text{dedtc})_3$ (0.2 mmol; 0.1133 g) and OAm (5 mL) to 50 °C under argon. To this, a hot mixture of $\text{Cu}(\text{acac})_2$ (0.2 mmol; 0.0524 g) and OAm (5 mL) was quickly injected followed by rapid heating to the respective nanostructure growth temperature (60, 70 or 200 °C) for 30 minutes. Aliquots of as-synthesized nanostructures at various time intervals were prepared from 0.1 mL of the reaction mixture and 1 mL of toluene for optical spectroscopy. As-synthesized nanostructures were purified by solvent-precipitation, i.e., centrifuged in acetone, isolated, and later stored as solid or sonicated and dispersed in toluene. For growth involving ODE, an additional 5 mL ODE was added to the mixture of $\text{Cu}(\text{acac})_2$ (0.2 mmol; 0.0524 g) and OAm (5 mL) followed by injection of this solution into the $\text{Sb}(\text{dedtc})_3$ mixture, rapid heating to 70 °C, and particle growth for 2, 5, 10 and 30 minutes, respectively. Also, for growth involving elemental sulphur, 1.3 mmol (0.0417 g) was added to the mixture of $\text{Cu}(\text{acac})_2$ (0.2 mmol; 0.0524 g) and OAm (5 mL) followed by injection of this solution into the $\text{Sb}(\text{dedtc})_3$ mixture, with rapid heating to 200 °C, and nanostructure growth for 30 minutes.

Measurements

For structural and optical spectroscopic analyses, nanostructures as a toluene ink were drop-casted onto single side polished (111) silicon wafer or quartz substrates, allowed to dry and mounted onto sample holders. X-ray diffractograms were obtained using a Rigaku SmartLab diffractometer with filtered $\text{Cu-K}\alpha$ radiation ($\lambda = 0.15406\ \text{nm}$) within a 2 θ range of 20 to 60 ° and step size of 0.1 °/second for 1½ hours, operating at 44 mA and 40 kV. Diffractograms were auto-indexed using the ExPO 2014 software.⁶¹ Raman spectroscopy was carried out using a Horiba XploRA microRaman spectrometer – confocal Raman microscope system at a laser excitation wavelength of 532 nm and a Peltier-cooled CCD camera. Single crystal Si was used to calibrate the Raman acquisitions with a typical Raman peak at 520.6 cm^{-1} and spectra recorded with a 100x objective lens within the range 100 – 1000 cm^{-1} . X-ray photoelectron spectroscopy (XPS) was conducted using a Multi-probe X-ray photoelectron spectrometer with a pass energy of 20 or 50 eV,

ARTICLE

Journal Name

10 mA emission, 15 kV bias on the Al K α (1487 eV) anode and step size of 0.10 or 0.05 °/second. Sputtering ion beam at 2 keV was used for 10 minutes. For Gaussian peak fitting, OriginPro⁶² was used with a Gaussian spline background. Samples were flooded with low-energy electrons for efficient charge neutralization. Binding energies were determined using C 1s at 284.8 eV as the charge reference. For transmission electron microscopy (TEM), nanostructures as a dilute toluene suspension were drop-casted onto nickel grids, allowed to dry and mounted onto sample holders. Microscopic images were captured using a Philips EM 420 TEM instrument with an accelerating voltage of 100 kV. High-resolution transmission electron microscopy was carried out using a FEI Talos F200X scanning (S/TEM) microscope at 200 keV, and energy dispersive spectroscopic data recorded to deduce elemental composition with electron beam accelerating voltage of 20 keV as well as selected area electron diffraction (SAED) and fast Fourier transform (FFT) diffraction. Size distributions were evaluated by measuring >100 particles per sample with ImageJ software.⁶³ Absorption spectra of nanostructures were recorded with a Perkin Elmer Lambda 950 UV/vis spectrometer within the range, 200 – 800 nm. Photoluminescence emission spectra were recorded using the Perkin Elmer LS55 fluorescence spectrometer with excitation wavelength of 335 nm within the region of 300 – 900 nm. Time-resolved photoluminescence measurements were done using a time-correlated-single-photon-counting laser setup. This included the Picoquant FT 200 spectrometer, a Hamamatsu microchannel plate-photomultiplier tube (PMT) detector for UV-vis (25 ps response) and a Hamamatsu InGaAs PMT for NIR (400 ps response). Electrochemical analyses were carried out using a three-electrode setup of fCAS nanostructured coated stainless-steel working electrode, platinum sheet counter electrode and Ag/AgCl reference electrode in 1 M Na₂SO₄ electrolyte. The electrochemical performance of fCAS nanostructured electrodes were investigated via cyclic voltammetry in the range of -1.1 to 0.5 V over several scan rates and electrochemical impedance spectroscopy in the frequency range of 1 to 1x10⁵ Hz at two fixed potentials of 0.0 and 0.5 V. The Nyquist plots were fitted using the Randles equivalent circuit model. In particular, the semicircle section of the plots was fitted using the Levenberg-Marquardt iteration algorithm (OriginPro) according to the equation: $y = y_0 + (((r^2) - (x - x_0)^2))^{1/2}$ to give a measure of the bulk conductivity (R_b) of the electrodes (R_s + R_{ct}). The working electrode was prepared by grinding a 80:15:5 mixture of the active material (fCAS nanostructures), carbon black, and PVDF with an appropriate amount of NMP solvent to form a uniform slurry which was coated onto a pre-cleaned stainless-steel substrate (2 x 1 cm) and allowed to dry at 50 °C.¹⁴ The electroactive mass of the fCAS electrode is 5 mg, calculated from the difference between the mass of the substrate before and after coating. Fourier transform Infrared (FTIR) spectrum of the diethyldithiocarbamate precursor was collected between 650 and 4000 cm⁻¹ using a Perkin Elmer Thermo Scientific ID5-ATR spectrometer. The proton and carbon nuclear magnetic resonance spectroscopies of the

diethyldithiocarbamate precursors were conducted using a Bruker Avance III 600 MHz spectrometer.

Conclusion

In this study, off-stoichiometric famatinite phase copper antimony sulphide (fCAS) colloidal nanostructures (2.4 – 18.0 nm) were grown under variable conditions of low and high temperatures (60 – 200 °C), time and oleylamine capping ligand concentration using copper(II) acetylacetone and antimony(III) diethyldithiocarbamate precursors. These fCAS colloidal quasi-spherical nanospheres and quasi-hexagonal nanostructures (including nanosheets) exhibit a correlation of particle size, morphology and composition with oleylamine concentration, growth time, and growth temperature. The off-stoichiometric nanostructures are severely copper-poor and antimony-rich in which copper vacancies, deep-lying donors of antimony interstitials and vacancies of sulphur, and copper-antimony antisites as deep-lying acceptors and surface trapping states are likely implicated in broad vis-NIR photoluminescence with fast recombination of short radiative lifetimes between 0.2 and 6.2 ns, and composition-dependent UV-visible absorption and tunable bandgaps between ~2.4 and 2.8 eV. Electrochemical analysis using a three-electrode configuration reveals that the charge storage mechanism in fCAS nanostructured working electrode occurs mainly via the surface adsorption of Na⁺ electrolyte ions and their intercalation indicating the pseudocapacitive nature of fCAS nanostructures. Overall, the tunable properties of the fCAS nanostructures, in terms of particle size, composition, morphology, and intrinsic defect states, achieved through variable conditions of colloidal growth uncover their potential for a range of applications such as photovoltaics, optoelectronics and pseudocapacitive electrodes for energy storage devices.

Author contributions

Kimberly Weston: investigation, data curation, writing draft preparation, writing-reviewing, and editing. Richard A. Taylor: writing-reviewing and editing, supervision, visualization, conceptualization. David Hinds: data collection. Kim Kisslinger: data collection. Shobha Mantripragada: data collection.

Conflicts of interest

There are no conflicts to declare.

Data availability

Data for this article are available at [name of repository] at [URL – format <https://doi.org/DOI>]. The data supporting this article have been included as part of the Supplementary Information.

Acknowledgements

The authors extend thanks to the Department of Chemistry, Department of Physics (Electron Microscopy Unit), School for Graduate Studies and Research as well as the Office of the Dean, Faculty of Science and Technology, University of the West Indies, St. Augustine campus and Office of Diversity Equity and

Journal Name

ARTICLE

Inclusion, Brookhaven National Laboratory for financial assistance. This research was partly conducted using facilities of the Center for Functional Nanomaterials, which is a U.S. Department of Energy Office of Science User Facility, at Brookhaven National Laboratory under Contract No. DE-SC0012704, as well as the Joint School of Nanoscience and Nanoengineering of North Carolina A&T State University, a member of the Southeastern Nanotechnology Infrastructure Corridor (SENIC) and National Nanotechnology Coordinated Infrastructure (NNCI), which is supported by the National Science Foundation (ECCS-2025462).

Notes and references

1. C. Coughlan, M. Ibáñez, O. Dobrozhana, A. Singh, A. Cabot and K. M. Ryan, *Chemical Reviews*, 2017, **117**, 5865-6109.
2. P. Baláž, E. Guilmeau, N. Daneu, O. Dobrozhana, M. Baláž, M. Hegedus, T. Barbier, M. Achimovičová, M. Kaňuchová and J. Briančin, *Journal of the European Ceramic Society*, 2020, **40**, 1922-1930.
3. D. Xu, S. Shen, Y. Zhang, H. Gu and Q. Wang, *Inorganic Chemistry*, 2013, **52**, 12958-12962.
4. K. Ramasamy, H. Sims, W. H. Butler and A. Gupta, *Chemistry of Materials*, 2014, **26**, 2891-2899.
5. F. Makin, F. Alam, M. A. Buckingham and D. J. Lewis, *Scientific Reports*, 2022, **12**, 5627.
6. G. H. Albuquerque and G. S. Herman, 2016.
7. S. Banu, S. J. Ahn, S. K. Ahn, K. Yoon and A. Cho, *Solar Energy Materials and Solar Cells*, 2016, **151**, 14-23.
8. T. Rath, A. J. MacLachlan, M. D. Brown and S. A. Haque, *Journal of Materials Chemistry A*, 2015, **3**, 24155-24162.
9. L. Yu, R. S. Kokenyesi, D. A. Kesler and A. Zunger, *Advanced Energy Materials*, 2013, **3**, 43-48.
10. Y. Rodríguez-Lazcano, M. T. S. Nair and P. K. Nair, *Journal of The Electrochemical Society*, 2005, **152**, G635.
11. C. Tablero, *The Journal of Physical Chemistry C*, 2014, **118**, 15122-15127.
12. Q. Zeng, Y. Di, C. Huang, K. Sun, Y. Zhao, H. Xie, D. Niu, L. Jiang, X. Hao, Y. Lai and F. Liu, *Journal of Materials Chemistry C*, 2018, **6**, 7989-7993.
13. S. Fleischmann, J. B. Mitchell, R. Wang, C. Zhan, D.-e. Jiang, V. Presser and V. Augustyn, *Chemical Reviews*, 2020, **120**, 6738-6782.
14. S. Sahoo, K. Krishnamoorthy, P. Pazhamalai, V. K. Mariappan and S. J. Kim, *International Journal of Hydrogen Energy*, 2018, **43**, 12222-12232.
15. C.-B. Chang, K.-T. Chen and H.-Y. Tuan, *Journal of Colloid and Interface Science*, 2022, **608**, 984-994.
16. V. K. Mariappan, K. Krishnamoorthy, P. Pazhamalai, S. Sahoo and S.-J. Kim, *Electrochimica Acta*, 2018, **275**, 110-118.
17. J. van Embden and Y. Tachibana, *Journal of Materials Chemistry*, 2012, **22**, 11466-11469.
18. J. van Embden, K. Latham, N. W. Duffy and Y. Tachibana, *Journal of the American Chemical Society*, 2013, **135**, 11562-11571.
19. S. Ikeda, S. Sogawa, Y. Tokai, W. Septina, T. Harada and M. Matsumura, *RSC Advances*, 2014, **4**, 40969-40972.
20. C. Yan, Z. Su, E. Gu, T. Cao, J. Yang, J. Liu, F. Liu, Y. Lai, J. Li and Y. Liu, *RSC Advances*, 2012, **2**, 10481-10484.
21. P. Christian and E. Liu, *Polyhedron*, 2010, **29**, 691-696.
22. J. C. Sarker and G. Hogarth, *Chemical Reviews*, 2021, **121**, 6057-6123.
23. S.-K. Ming, R. A. Taylor, P. D. McNaughton, D. J. Lewis, M. A. Leontiadou and P. O'Brien, *RSC Advances*, 2021, **11**, 21351-21358.
24. S.-K. Ming, R. A. Taylor, P. D. McNaughton, D. J. Lewis and P. O'Brien, *New Journal of Chemistry*, 2022, **46**, 18899-18910.
25. A. Pfitzner and S. Reiser, *Zeitschrift für Kristallographie - Crystalline Materials*, 2002, **217**, 51-54.
26. A. D. Prasetya, M. Rifai and H. Miyamoto, 2020.
27. D. Baranov, M. J. Lynch, A. C. Curtis, A. R. Carollo, C. R. Douglass, A. M. Mateo-Tejada and D. M. Jonas, *Chemistry of Materials*, 2019, **31**, 1223-1230.
28. L. Li, Y. Zhang, S. Xia, Z. Sun, J. Yuan, D. Su, H. Cao, X. Chai, Q. Wang, J. Li and Z. Zhang, *Microelectronics International*, 2023, **40**, 132-139.
29. C. Barnes, *Journal*, 2003.
30. C. E. HOUSECROFT, *Vibrational spectroscopy*, 2012, **71**, 3.7.
31. T. Alqahtani, M. D. Khan, D. J. Lewis, X. L. Zhong and P. O'Brien, *Scientific Reports*, 2021, **11**, 1887.
32. A. A. Rahman, E. Hossian, H. Vaishnav, J. B. Parmar, A. Bhattacharya and A. Sarma, *Materials Advances*, 2020, **1**, 3333-3338.
33. X. Fontané, V. Izquierdo-Roca, E. Saucedo, S. Schorr, V. O. Yukhymchuk, M. Y. Valakh, A. Pérez-Rodríguez and J. R. Morante, *Journal of Alloys and Compounds*, 2012, **539**, 190-194.
34. K. Weston, R. A. Taylor, B. C. Samuels, S. Taqy and R. Droopad, *Thin Solid Films*, 2024, **797**, 140345.
35. M. C. Biesinger, *Surface and Interface Analysis*, 2017, **49**, 1325-1334.
36. J. A. Torres-Ochoa, D. Cabrera-German, O. Cortazar-Martinez, M. Bravo-Sánchez, G. Gomez-Sosa and A. Herrera-Gomez, *Applied Surface Science*, 2023, **622**, 156960.
37. M. Tamilselvan and A. J. Bhattacharyya, *ACS Applied Energy Materials*, 2018, **1**, 4227-4234.
38. R. S. Rahman, K. Asokan and M. Zulfequar, *The Journal of Physical Chemistry C*, 2022, **126**, 6065-6074.
39. M. Bella, C. Rivero, S. Blayac, H. Basti, M. C. Record and P. Boulet, *Materials Research Bulletin*, 2017, **90**, 188-194.
40. T. Pretto, F. Baum, G. Fernandes Souza Andrade and M. J. Leite Santos, *CrystEngComm*, 2021, **23**, 397-403.
41. F. Baum, T. Pretto, A. G. Brolo and M. J. L. Santos, *Crystal Growth & Design*, 2018, **18**, 6521-6527.
42. N. Shukla, C. Liu, P. M. Jones and D. Weller, *Journal of Magnetism and Magnetic Materials*, 2003, **266**, 178-184.
43. J. E. Jaffe and A. Zunger, *Physical Review B*, 1983, **28**, 5822-5847.
44. R. Chetty, A. Bali and R. C. Mallik, *Journal of Materials Chemistry C*, 2015, **3**, 12364-12378.
45. W. Lian, C. Jiang, Y. Yin, R. Tang, G. Li, L. Zhang, B. Che and T. Chen, *Nature Communications*, 2021, **12**, 3260.
46. B. Chen, H. Zhong, W. Zhang, Z. a. Tan, Y. Li, C. Yu, T. Zhai, Y. Bando, S. Yang and B. Zou, *Advanced Functional Materials*, 2012, **22**, 2081-2088.
47. S. L. Castro, S. G. Bailey, R. P. Raffaelle, Banger, K. K. and A. F. Hepp, *Journal of Physical Chemistry B*, 2004, **108**, 12429-12435.
48. D. H. Jara, S. J. Yoon, K. G. Stamplecoskie and P. V. Kamat, *Chemistry of Materials*, 2014, **26**, 7221-7228.
49. Z. Chen, C. Xie, F. Yang, L. Feng, X. Liang and W. Xiang, *Journal of Alloys and Compounds*, 2014, **594**, 107-113.
50. P. Ranga, A. Bhattacharyya, A. Chmielewski, S. Roy, N. Alem and S. Krishnamoorthy, *Applied Physics Letters*, 2020, **117**.
51. E. Wangila, C. Gunder, M. Zamani-Alavijeh, F. Maia de Oliveira, S. Kryvyyi, A. Sheibani, Y. I. Mazur, S.-Q. Yu and G. J. Salamo, *Crystals*, 2024, **14**, 724.

ARTICLE

Journal Name

52. D. Mora-Herrera and M. Pal, *Applied Physics A*, 2022, **128**, 1008.

53. X. H. Rui, N. Yesibolati, S. R. Li, C. C. Yuan and C. H. Chen, *Solid State Ionics*, 2011, **187**, 58-63.

54. S. Dai, L. Wang, M. Cao, Z. Zhong, Y. Shen and M. Wang, *Materials Today Energy*, 2019, **12**, 114-128.

55. S. Sugarthi, V. S. Manikandan, S. Harish, G. Bakiyaraj and M. Navaneethan, *Journal of Materials Science: Materials in Electronics*, 2022, **33**, 9650-9659.

56. K. Ramasamy, R. K. Gupta, H. Sims, S. Palchoudhury, S. Ivanov and A. Gupta, *Journal of Materials Chemistry A*, 2015, **3**, 13263-13274.

57. S. T. Senthilkumar, R. K. Selvan, J. S. Melo and C. Sanjeeviraja, *ACS Applied Materials & Interfaces*, 2013, **5**, 10541-10550.

58. An, Tang, Q. Yang and Qian, *Inorganic Chemistry*, 2003, **42**, 8081-8086.

59. I. I. Ozturk, C. N. Banti, N. Kourkoumelis, M. J. Manos, A. J. Tasiopoulos, A. M. Owczarzak, M. Kubicki and S. K. Hadjikakou, *Polyhedron*, 2014, **67**, 89-103.

60. J. R. Castro, K. C. Molloy, Y. Liu, C. S. Lai, Z. Dong, T. J. White and E. R. T. Tieckink, *Journal of Materials Chemistry*, 2008, **18**, 5399-5405.

61. C. C. A. Altomare, C. Giacovazzo, A. Moliterni, R. Rizzi, N. Corriero and A. Falcicchio, *Journal of Applied Crystallography*, 2013, **46**, 1231-1235.

62. O. P. Origin(Pro), Northampton, MA, USA, Version 2018.

63. C. A. Schneider, W. S. Rasband and K. W. Eliceiri, *Nature Methods*, 2012, **9**, 671-675.

Data Availability Statement

The data supporting this article have been included as part of the Supplementary Information.